nuclear fusion
IAEA

PAPER • OPEN ACCESS

Model-based impurity emission front control using deuterium fueling and nitrogen seeding in TCV

To cite this article: J.T.W. Koenders *et al* 2023 *Nucl. Fusion* **63** 026006

View the article online for updates and enhancements.

You may also like

- SDSS-IV MaNGA: pyPipe3D Analysis Release for 10,000 Galaxies
S. F. Sánchez, J. K. Barrera-Ballesteros, E. Lacerda et al.
- Progress toward divertor detachment on TCV within H-mode operating parameters
J R Harrison, C Theiler, O Février et al.
- An Overview of the Dwarf Galaxy Survey
S. C. Madden, A. Rémy-Ruyer, M. Galametz et al.

This content was downloaded from IP address 1.27.104.22 on 03/11/2023 at 09:40

OPEN ACCESS
IOP Publishing | International Atomic Energy Agency
Nuclear Fusion
Nucl. Fusion **63** (2023) 069501 (2pp)
https://doi.org/10.1088/1741-4326/accfac

Corrigendum: Model-based impurity emission front control using deuterium fueling and nitrogen seeding in TCV (2023 *Nucl. Fusion* 63 026006)

J.T.W. Koenders[1,2,*], A. Perek[3], B. Kool[1,2], O. Février[3], T. Ravensbergen[4], C. Galperti[3], B.P. Duval[3], C. Theiler[3], M. van Berkel[1], the TCV Team[a] and the EUROfusion MST1 Team[b]

[1] DIFFER—Dutch Institute for Fundamental Energy Research, Eindhoven, Netherlands
[2] Department of Mechanical Engineering, Control Systems Technology Group, Eindhoven University of Technology, Eindhoven, Netherlands
[3] École Polytechnique Fédérale de Lausanne (EPFL), Swiss Plasma Center (SPC), Lausanne, Switzerland
[4] ITER Organization, St. Paul Lez Durance Cedex, France

E-mail: j.t.w.koenders@differ.nl

Received 3 April 2023
Accepted for publication 24 April 2023
Published 12 May 2023

Abstract
In the published paper titled 'Model-based impurity emission front control using deuterium fueling and nitrogen seeding in TCV' (2023 *Nucl. Fusion* **63** 026006), the legend of figure 5 shows the wrong colors: red and blue are switched. This corrigendum provides the correct legend for figure 5.

(Some figures may appear in colour only in the online journal)

[a] See Reimerdes *et al* 2022 (https://doi.org/10.1088/1741-4326/ac369b) for the TCV Team.
[b] See Labit *et al* 2019 (https://doi.org/10.1088/1741-4326/ab2211) for the EUROfusion MST1 Team.
[*] Author to whom any correspondence should be addressed.

Original Content from this work may be used under the terms of the Creative Commons Attribution 4.0 licence. Any further distribution of this work must maintain attribution to the author(s) and the title of the work, journal citation and DOI.

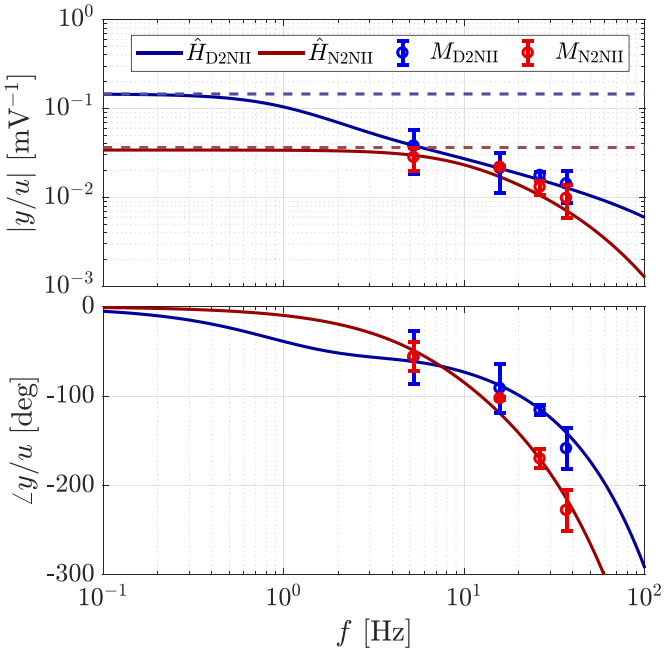


Figure 5. Bode plot of the transfer function models $\hat{H}_{\mathrm{N2NII}}(s)$ and $\hat{H}_{\mathrm{D2NII}}(s)$ and the FRF measurements of the full system from u (gas valve reference) to y (NII front position) in the case of D_2 and N_2 gas perturbation, indicated by $M_{\mathrm{D2NII}}(s)$ and $M_{\mathrm{N2NII}}(s)$ respectively. The dashed lines indicate the DC-gain used to regress the $G(s)$ models multiplied by the DC-gain of the valve and sensor, i.e. $\hat{H}_{\mathrm{N2NII}}(0)$ and $\hat{H}_{\mathrm{D2NII}}(0)$.

Acknowledgments

DIFFER is part of the institutes organization of NWO.

This work was supported in part by the Swiss National Science Foundation.

This work has been carried out within the framework of the EUROfusion Consortium, funded by the European Union via the Euratom Research and Training Programme (Grant Agreement No. 101052200—EUROfusion). Views and opinions expressed are however those of the author(s) only and do not necessarily reflect those of the European Union or the European Commission. Neither the European Union nor the European Commission can be held responsible for them.

ORCID iDs

J.T.W. Koenders https://orcid.org/0000-0003-4385-923X
A. Perek https://orcid.org/0000-0002-4117-0298
B. Kool https://orcid.org/0000-0002-1636-7400
O. Février https://orcid.org/0000-0002-9290-7413
T. Ravensbergen https://orcid.org/0000-0001-7347-5515
C. Theiler https://orcid.org/0000-0003-3926-1374
M. van Berkel https://orcid.org/0000-0001-6574-3823

OPEN ACCESS
IOP Publishing | International Atomic Energy Agency
Nuclear Fusion
Nucl. Fusion **63** (2023) 026006 (11pp)
https://doi.org/10.1088/1741-4326/aca620

Model-based impurity emission front control using deuterium fueling and nitrogen seeding in TCV

J.T.W. Koenders[1,2,*], A. Perek[3], B. Kool[1,2], O. Février[3], T. Ravensbergen[4], C. Galperti[3], B.P. Duval[3], C. Theiler[3], M. van Berkel[1], The TCV Team[a] and The EUROfusion MST1 Team[b]

[1] DIFFER—Dutch Institute for Fundamental Energy Research, Eindhoven, Netherlands
[2] Department of Mechanical Engineering, Control Systems Technology Group, Eindhoven University of Technology, Eindhoven, Netherlands
[3] École Polytechnique Fédérale de Lausanne (EPFL), Swiss Plasma Center (SPC), Lausanne, Switzerland
[4] ITER Organization, St. Paul Lez Durance Cedex, France

E-mail: j.t.w.koenders@differ.nl

Received 31 August 2022, revised 11 November 2022
Accepted for publication 25 November 2022
Published 20 December 2022

Abstract

This paper presents the first result using nitrogen-seeded exhaust feedback control of the NII impurity emission front in TCV. The NII emission front position is consistently located below its commonly used CIII counterpart, indicating the NII emission front is representative of a colder plasma region. We demonstrate control of the NII impurity emission front position for two cases: (a) using nitrogen seeding as the sole actuator, and (b) using deuterium fueling as an actuator while injecting a small amount of nitrogen that remains a trace impurity. For sole nitrogen actuation, peak target current density is significantly reduced when the NII emission front approaches the x-point (≈50% for the NII front at the halfway point). When actuating with deuterium, peak target current density is less affected, which is explained by changes in fueling engendering a different scrape-off-layer plasma density. Perturbative (system identification) experiments show that nitrogen actuation induces a stronger, but slower, response of the NII emission front than deuterium actuation. Moving the NII emission front back to the target after pushing it towards the x-point has proven difficult, where both the NII front position and total radiated power do not reach pre-seeding conditions within the discharge time following termination of nitrogen injection. This result highlights the need to account for impurity retention for such seeded discharges in exhaust control strategies.

Keywords: power exhaust, detachment control, system identification, impurity seeding, TCV

(Some figures may appear in colour only in the online journal)

[a] See author list of Reimerdes *et al* 2022 *Nucl. Fusion* 62 042018.
[b] See author list of Labit *et al* 2019 *Nucl. Fusion* 59 086020.
[*] Author to whom any correspondence should be addressed.

Original Content from this work may be used under the terms of the Creative Commons Attribution 4.0 licence. Any further distribution of this work must maintain attribution to the author(s) and the title of the work, journal citation and DOI.

1. Introduction

One of the major outstanding challenges for reactor relevant tokamak operation is the heat and particle load on the first wall, notably the divertor [1]. Left unmitigated, the expected power fluxes impacting the divertor targets during reactor-relevant operation exceed present-day materials engineering limits [2, 3]. Real-time feedback control of plasma detachment, a regime characterized by a large reduction of plasma temperature and plasma pressure at the divertor target, is required to maintain a sufficient reduction of these fluxes [4, 5].

Designing such exhaust feedback controllers systematically requires a dynamic (time-dependent) model of the to-be-controlled physical system. This model includes the plasma, actuator, and sensor, and allows to design for model-based guarantees on stability and performance of the controlled system [6]. Predictive dynamic models are therefore paramount to confidently apply controllers to a new reactor from the first discharge. This should start with a robust design in the robustness-performance trade-off, and move to performance design once more experimental data is available to improve the modeled dynamics. Experimental identification of the heat exhaust dynamics is therefore the logical approach to design controllers for present-day devices. This ensures a discharge efficient control development and adds dynamic data to the experimental database necessary for validating first-principle time-dependent models.

In [7], dedicated *system identification* experiments were performed to obtain a parametric dynamic model of the CIII (465 nm triplet) emission front position response to deuterium (D_2) fueling in the carbon machine Tokamak à configuration vriable (TCV). This model was used to systematically design a controller off-line. This approach resulted in a successful real-time feedback control of the CIII emission front, where the intrinsic Carbon of the TCV wall allowed for enhanced radiation. In future reactors, i.e. metal walls, intrinsic impurity radiation from carbon will not be present. Therefore, exhaust control will require the direct injection of impurities into the divertor region to augment power losses, as is envisioned for ITER and DEMO [8, 9].

In this paper, we adhere to this approach, performing real-time plasma exhaust control with the direct injection of nitrogen (N_2) in TCV. N_2 is injected through a piezo-electric gas valve into the divertor to further cool the exhaust plasma. We employ the resulting NII (399.5 nm) emission front to diagnose the plasma detachment progression. Similarly to carbon, nitrogen has a high radiative potential for the temperature range typical of the TCV divertor. We use the transfer function structure derived in [10] for emission front control in TCV, which is based on a 1D diffusion equation. This model is regressed against system identification measurements, because the simple gain and delay model used in [7] was unable to reproduce the measured dynamic response of the CIII emission front to D_2 gas injection [10].

Note that, the corresponding nitrogen seeded detachment physics in TCV L-mode plasmas was probed experimentally in [11] and compared with SOLPS-ITER in [12]. In this paper we focus specifically on using the NII emission front position as a control parameter for the divertor plasma and designing corresponding controllers. Furthermore, we compare the dynamic response of the exhaust plasma to N_2 and D_2 injection to gain further insight in the dynamic modeling for heat exhaust control.

In this paper, we report on three key results. (a) Successful real-time control of the NII emission front position actuated by both N_2 and D_2, which includes using N_2 as a tracer. A single discharge per actuator was sufficient to identify the transfer function model parameters and design a controller for each of these: N_2 and D_2. This is the first demonstration of real-time control of the plasma exhaust using N_2 in TCV. This is also the first demonstration of using the transfer function structure of [10] to design a gas injection actuated emission front controller. (b) The controlled NII front position was consistently located 2–3 cm below the CIII emission front position. Hence, we conclude that the NII emission is indicative of a colder region than the CIII emission. This is qualitatively in line with the SOLPS-ITER analysis of [12], where the CIII and NII impurity emission fronts were found to correspond to local electron temperatures of 11–12 and 6.5 eV, respectively. Note that the experimental temperatures (from spectroscopy and Thomson Scattering when available) are generally considerably lower for both (see e.g. [13] and references therein). (c) The CIII and NII emission front positions respond identically to D_2 or N_2 injection perturbations in the system identification experiments. This indicates they cannot be controlled independently by the used actuators, at least up to the highest excited frequency of 37 Hz. Both fronts do, however, respond differently to actuation using D_2 than to actuation using N_2, with the latter inducing a stronger, but slower response of both fronts.

This paper is organized as follows. In section 2, the experimental set-up and the control goal, including the used actuators and sensor in the control loop are introduced. In section 3, the system identification experiments are discussed and their results presented. The system identification results are then used to regress the diffusion-based transfer function structure on which we base the controller design. We show the emission front control results in section 4, and analyze the impact of NII emission front position on target saturation current density and radiated power fraction. We also compare actuation of the NII emission front using D_2 and N_2 as actuators to track the same desired reference position. The conclusions and a discussion follows in section 5.

2. Experimental setup

The experiments for this work were performed on the TCV [14]. Results are obtained in a lower single-null 340 kA Ohmically heated diverted L-mode scenario in reversed field (unfavorable to H-mode access), $B_{\mathrm{tor}} = 1.4$ T, and a line-averaged electron density of $\hat{n}_{\mathrm{e}} \approx 9 \times 10^{19}\,\mathrm{m}^{-3}$ ($f_{\mathrm{GW}} = 0.4$). The scenario is similar to the high-density scenario used in [11] to analyze nitrogen seeded divertor detachment in TCV L-mode plasmas and was chosen as it operates close to detachment. Additionally, it was observed in [11] that the higher

line-averaged density case resulted in better core screening to N_2 penetration, increasing the discharge's operational range with respect to the quantity of N_2 injected.

2.1. Control goal

The TCV divertor plasma can be spectroscopically diagnosed from either intrinsic (e.g. carbon, helium, hydrogen) or extrinsic (e.g. nitrogen, argon) line emission [15, 16]. Their emission spectra are strongly temperature-dependent in the divertor plasma temperature range, providing direct information on the divertor plasma state [17].

In this work, we aim to control the NII emission front position, diagnosing the exhaust plasma by using the emission of an injected impurity instead of the intrinsic carbon always present in TCV. We aim to control the NII front with two actuators: (a) Using N_2 gas injection as an actuator, directly changing the impurity radiated power intensity whilst having a relatively small effect upon the core plasma density; (b) Using D_2 gas injection as an actuator, increasing the divertor plasma density which changes the intrinsic carbon source. These affect hydrogenic and carbon radiated power respectively. In case 2, we also inject a small amount of N_2, to probe the use of extrinsic impurities as diagnostic tracers. For this work we define the tracer impurity as a relatively small amount of N_2 injection, not used as an actuator for control. The chosen amount resulted in a relatively constant measurement of integrated NII emission showing only minor impurity content build-up. We note that changes in integrated NII emission may be an incomplete measure of changes in nitrogen concentration in the divertor plasma, but use it as an estimate.

The receding of CIII emission from the target is often taken as an indication of the onset of divertor detachment in TCV [11, 13, 18, 19] and was used as a control parameter cast as an emission front position in [7]. The NII impurity emission front has not yet been used for control purposes, and may have different characteristics as a control parameter.

From SOLPS-ITER analysis of [12] and experimental results from [11] the NII emission front position is expected at a lower plasma temperature and therefore positioned between the divertor target and the CIII emission front position. Its receding from the target is thus an indication of lower divertor temperatures than the receding of CIII emission. It may be reasonable to expect that the dynamic response of the NII emission front position to N_2 is considerably different than that of the CIII emission front, as in the first case the emitting impurity is directly used for actuation while in the second case it is related to the intrinsic carbon source. However, we will show that both the NII emission front and CIII emission front respond identically to perturbations of a single gas species, be it N_2 or D_2.

Figure 1 shows the process control loop. The dynamics of the full system H are defined from requested gas input u to measured NII front position y, that includes the actuator A, the plant G and sensor S. These need to be included to design a feedback controller off-line and predict performance and robustness margins [20]. Next, we elaborate on the used sensor and actuator and their individual dynamics. Identification of

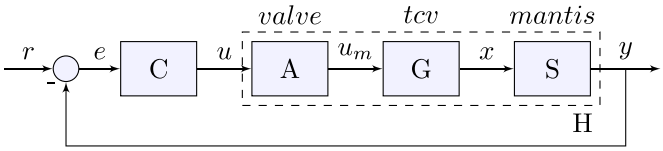


Figure 1. The process control loop. A control reference position r is compared with a measured front position y. The control error e is fed to a controller C, which computes voltage request u, send to the gas valve actuator A. The internal gas valve controller follows this request, resulting in a (measured) injected gas flow u_{m}. The gas enters the plant G, which is the TCV. The divertor plasma response, in terms of an emission front position, is measured using the sensor S, i.e. MANTIS.

the local (linearized) dynamics of the plant G, together with the full system from u to y, is performed through system identification experiments shown in section 3.

2.2. Sensors

The NII and CIII emission front locations are measured using a real-time detection algorithm [21] applied to spectrally filtered images originating from the multi-spectral imaging diagnostic MANTIS [22]. The MANTIS cameras run at a frame rate of 800 Hz, where the shutter opening time stamp plus half the exposure time (≈0.5 ms) for each image is taken as the representative time for when each image, and thus the front position, is measured. We define the corresponding front position as x_{NII}, which is the total distance from the outer divertor target to the front location, along the outer leg. Conversely, the front position as received by the real-time control system, after the image has traversed the real-time detection and written the result to memory, is defined as y_{NII}. The value for y_{NII} is delayed by 4 ms with respect to x_{NII}. These sensor dynamics S are, thus, well captured by $y(t+0.004) = x(t)$. We will transform these sensor dynamics to the Laplace domain, since the total system then becomes a straightforward multiplication of the terms: $G(s) = S(s)H(s)A(s)$, assuming local linearity. This was elaborated in previous work [10] and references therein. The sensor dynamics $y(t+0.004) = x(t)$ then become the transfer function

$$y(s) = \underbrace{\mathrm{e}^{-0.004s}}_{S(s)} x(s), \tag{1}$$

with s the Laplace variable.

We investigate the effect of the NII emission front position on the divertor plasma from the ion saturation current density at the inner- and outer strike points using wall- embedded Langmuir probes, and from the radiated power measured by gold-foil bolometers [23]. The Langmuir probes provide a measurement of the ion saturation current density from current–voltage curve fits over a 5 ms period average (further details on the analysis are described in [24]). The bolometers estimate the total radiated power fraction $f_{\mathrm{rad}}^{\mathrm{tot}}$ and radiated power fraction in the scrape-off-layer $f_{\mathrm{rad}}^{\mathrm{SOL}}$. Radiated power from the core $P_{\mathrm{rad}}^{\mathrm{core}}$ is estimated from a tomographic reconstruction of the bolometer camera array. We define the total and SOL radiated power fractions as

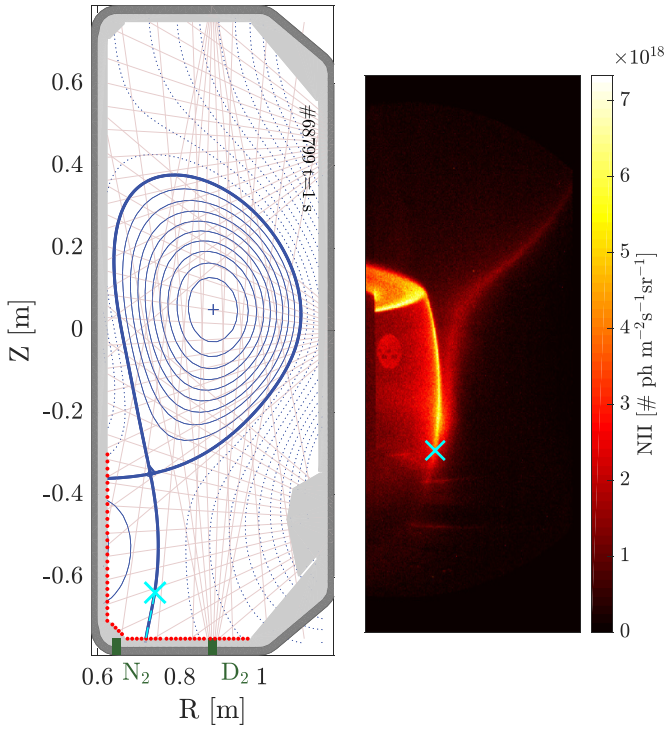


Figure 2. *Left:* magnetic geometry used for this work is shown in the poloidal plane of TCV in blue. Langmuir probe locations which were used to measure ion saturation current density are shown by red dots. Lines of sight of 64 gold-foil bolometers which were used to estimate radiated power are shown in pink. Gas injection locations of D_2 and N_2 are located at the machine bottom shown in dark green. *Right:* NII emission image from MANTIS at $t = 1$ s during this discharge, including the detected NII emission front location indicated by the cyan cross. The detected position is mapped to the poloidal plane on the left using the algorithm of [21], resulting in $y_{\mathrm{NII}} = 0.12$ m, which is the total distance from the outer divertor target to the front position along the outer leg.

$$f_{\mathrm{rad}}^{\mathrm{tot}} = \frac{P_{\mathrm{rad}}^{\mathrm{tot}}}{P_{\mathrm{ohm}}}, \qquad f_{\mathrm{rad}}^{\mathrm{SOL}} = \frac{P_{\mathrm{rad}}^{\mathrm{tot}} - P_{\mathrm{rad}}^{\mathrm{core}}}{P_{\mathrm{ohm}} - P_{\mathrm{rad}}^{\mathrm{core}}} = \frac{P_{\mathrm{rad}}^{\mathrm{SOL}}}{P_{\mathrm{SOL}}}, \tag{2}$$

respectively, where P_{ohm} is the ohmic heating power. Figure 2 shows the positions of the LPs, bolometer lines of sight, and an example of the detected NII emission front position a discharge.

2.3. Actuators

The NII emission front position is controlled by the injection of N_2 or D_2 molecules in the divertor through piezo-electric gas valves [25]. A pressure transducer at the output of the valve is absolutely calibrated to estimate the mass flow entering the vacuum vessel. Both the actuator voltage request u to the valve, and the pressure at the valve output (directly related to gas flow) u_{m} are measured. The piezo-electric valves have a dynamic response from a requested gas flow to an actual gas flow indicated by the block A in figure 1. Separate identification of the dynamics of each valve was obtained by step response measurements. Their dynamics were well captured by a first-order plus dead-time (FOPDT) model

$$\dot{u}_{\mathrm{m}}(t)\tau = -u_{\mathrm{m}}(t) + Ku(t - \tau_d), \tag{3}$$

that can be described by the transfer function

$$u_{\mathrm{m}}(s) = \frac{K}{\tau s + 1} \mathrm{e}^{s\tau_d} u(s), \tag{4}$$

with model parameters K [-], τ [s] and τ_d [s] that describe the system gain, time constant and delay respectively. The step response of (3) is

$$u_{\mathrm{m}}(t) = \delta K(1 - \mathrm{e}^{(t-\tau_d)/\tau}), \tag{5}$$

where δ is the applied step input on u. The model parameters K, τ and τ_d are determined by regressing the FOPDT model on 15 step response measurements in the time-domain, using a root-mean-squared error minimization of the modeled step-response with respect to the measured response.

Table 1. Gas valve model parameters.

Parameter	N_2 valve	D_2 valve	Unit
K	0.91	0.97	—
τ	2.00	1.12	ms
τ_d	1.90	1.50	ms

Table 1 shows the average of the obtained model parameters for each valve over the 15 measurements. We shall refer to the corresponding models as $A_{D2}(s)$ and $A_{N2}(s)$ for the deuterium valve and the nitrogen valve, respectively. Figure 2 shows the gas injection locations of both these valves in TCV.

3. System identification experiments

Efficient and systematic controller design requires a dynamic model of the to-be-controlled system [6], herein the total dynamics from input u to output y as shown in figure 1. In reality, most systems have non-linear input/output characteristics, however, a local linear description is often sufficient to describe the dynamics within a useful operating range [26], where the feedback controller will deal with residual non-linearities. These local system dynamics are identified experimentally using dedicated system identification experiments, similar to [7, 27]. By exciting the system with carefully designed perturbations to the input u while measuring the output y, assuming small perturbations, a local linear approximation of the system is identified. This local description is only valid for an operating range around the perturbed equilibrium, whose size depends on the strength of present non-linearities. In [7] no clear non-linear contributions were identified from dedicated system identification experiments using D_2 gas perturbations to perturb the CIII emission front position, providing confidence that a local linear description is adequate for emission front controller design.

As described in section 2, we can measure the mass flow of gas entering the vessel, and also the shutter aperture time

of MANTIS and corresponding front position measurement x. We can therefore identify the local dynamics of the plant, $\hat{G}(s)$, individually as well as the local dynamics of the total system $\hat{H}(s) = A(s)\hat{G}(s)S(s)$. We will use this to compare the local response of the divertor plasma to D_2 and N_2 gas injection without including any spurious effects from the actuator or sensor dynamics, i.e. comparing the plant physics only. With the actuator and sensor dynamics $A(s)$ and $S(s)$ taken as global descriptions to be valid for the full operational space. For the gas valves known to be untrue when operating near its closure, as its response becomes nonlinear, but we shall assume this contribution to be negligible.

In the following section, the perturbation design for the system identification experiments is briefly discussed, and the experimental results are presented.

3.1. Perturbation design

We identify $\hat{H}(s)$ and $\hat{G}(s)$ in the form of frequency response function (FRF) data, obtained using sinusoidal perturbations superimposed on a pre-programmed feedforward trace. An FRF datapoint is obtained for each frequency ω [rad s^{-1}] excited in the perturbation waveform, consisting of the relative amplitude and relative phase of the measured output response to the input perturbation. The FRF datapoints are the evaluation of the system its transfer function in the Fourier domain using $s = j\omega$, which may be interpreted as its response to constant amplitude oscillations. The perturbation we apply to the gas input is a multisine waveform, consisting of a sum of sinusoids, each with a distinct frequency, phase and amplitude. Such a multisine waveform is chosen as all perturbation energy is then concentrated on the chosen set of frequencies, maximizing signal to noise ratio. Additionally, a key benefit of identifying the system with an FRF is that no pre-chosen model structure is required, i.e. no assumption on the underlying physics is made.

More information on the specific design of this approach with multisine perturbations in TCV experiments is described in [7], with more information on the general theory available in [27, 28].

The discharge scenario allows for a perturbation time τ_{exp} of approximately 0.8 s, placing a lower bound on the identifiable frequency range, or fundamental frequency f_0, at 3.75 Hz as a minimum of three periods is required to obtain a meaningful variance computation [28]. We choose to perturb the system using a multisine with $f_0 = 1/0.19$ Hz and harmonics on lines $1, 3, 5, 7$ (5.26, 15.79, 26.32, 36.84 Hz), applied to the N_2 valve and D_2 valve in discharges #68861 and #69147, respectively. A slightly higher frequency than 3.75 Hz is chosen such that earlier than expected plasma discharge termination would include at least three periods of perturbation, ensuring more discharges were effective.

3.2. Experimental results

Figure 3 shows the time traces of the two system identification discharges. The perturbations are superimposed on a designed feedforward trace that provides approximately

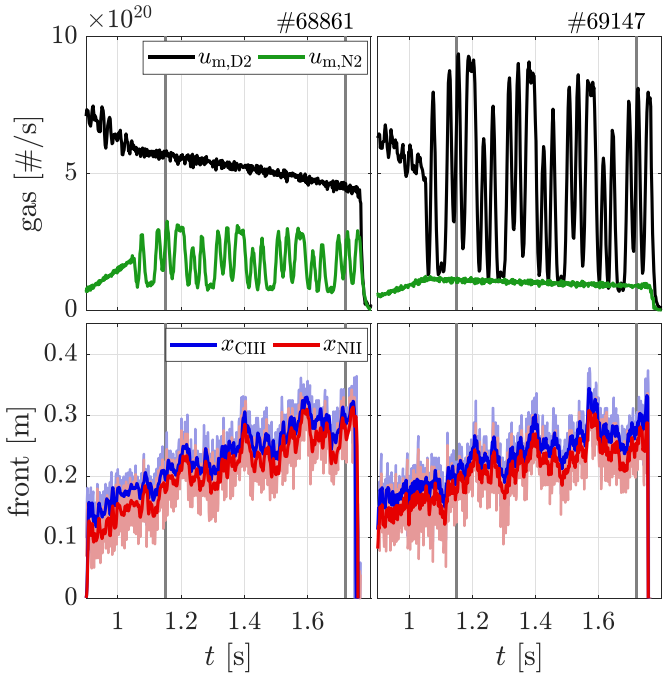


Figure 3. Time-traces of the system identification experiments for discharges #68861 *(left)* and #69147 *(right)*. *Top:* measured gas injection in molecules per second for both nitrogen ($u_{\mathrm{m,N2}}$) and deuterium ($u_{\mathrm{m,D2}}$). *Bottom:* measured impurity front position of CIII and NII compensated for the 4 ms time-delay of the sensor dynamics. A filtered measurement, using a IIR low pass filter with 40 Hz passband edge frequency, is shown on top of the raw measurement for clarity of the response in the time-domain.

constant line-averaged density. We observe a clear response of both the NII and CIII emission front to perturbations applied to the N_2 and D_2 valves, including a slow drift of the front position upward along the divertor leg towards the x-point. This drift is a transient response, likely caused by nitrogen content build-up in the plasma and/or changing wall sources and sinks, for which we compensate in the frequency domain analysis using the local polynomial method (LPM) [27, 29]. The LPM separates the measured transient response from the response originating from the excitation frequencies in the multisine perturbation. This exploits the property of transients to be smooth over frequency, unlike the response of the multisine excitation.

We find the CIII emission front position is consistently located 2–3 cm above the NII emission front position throughout the discharge, demonstrating the NII front is indicative of a colder region than for CIII assuming a negative temperature gradient from upstream to target.

We analyze the frequency response measurements by plotting the FRF datapoints in a Bode plot, that shows the relative amplitude and phase between input perturbation and output response. Figure 4 shows the measured FRF data points from both actuators (actual N_2 and D_2 gas flow) to the CIII and NII emission front positions compensated for the 4 ms measurement delay, i.e. these results are corrected for actuator and sensor dynamics (cf $G(s)$ only in figure 1).

The FRF data shows that both the CIII and NII emission fronts respond equally to the perturbations on a single actuator,

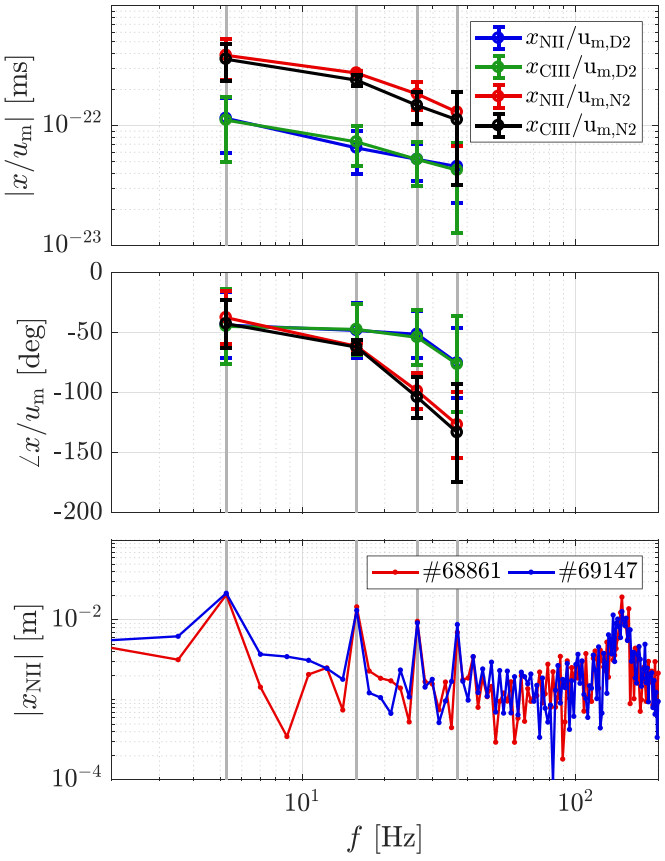


Figure 4. Results of the system identification experiments in the frequency domain. *Top and middle:* FRF measurement results of the CIII and NII emission front responses to nitrogen ($u_{\mathrm{m,N2}}$) and deuterium ($u_{\mathrm{m,D2}}$) shown in a Bode plot. Results are compensated for non-periodic behavior like transients using the local polynomial method as described in [27]. The 2σ errorbars are computed using the propagation of uncertainty for magnitude and phase as in [30], assuming a noiseless input case. *Bottom:* discrete Fourier transform (DFT) of the NII emission front response to both gas species, the signal has been compensated for the slow drift (using linear detrending) for clarity. The grey vertical lines indicate the excited frequencies in the perturbation.

i.e. they move together when a single gas species is perturbed. Until the highest probed excitation frequency of 36.84 Hz, no clear separation of these fronts is seen, implying emission equilibration time-scales in the scrape-off layer are significantly faster.

With N_2 perturbations, we observe a stronger phase drop and an amplitude response of almost a factor four higher, per molecule, than with D_2. Thus, N_2 injection results in a stronger, although for higher (>10 Hz) frequencies slower, response of the NII and CIII emission front positions than D_2. Generally, a smaller phase delay results in higher possible performance of the closed-loop system. The results indicate a higher performance may be possible with D_2 actuation of impurity emission front position, assuming there is no issue with the required larger gas injection amplitude.

Figure 4 also shows the discrete Fourier transform (DFT) of the NII emission front response amplitude over frequency. The perturbed frequency amplitudes are clearly well above the noise level, with a strong peak observed around ∼150 Hz. This periodic external disturbance (not resulting from the applied perturbations) is concentrated around the sawteeth crash frequency for this scenario, determined from soft x-ray emission measurements. Sawteeth perturb the core plasma, and are some time later observed in the divertor plasma. They do not effect the system identification results, as it is significantly removed from the probed excitation frequencies. However, this observation will be retained in controller design, to ensure it does not act on these high frequency disturbances.

In the next section we obtain a model of the full system H, by coupling the estimated actuator and sensor dynamics $A(s)$ and $S(s)$ to our local plant dynamics $\hat{G}(s)$. The resulting model $\hat{H}(s) = S(s)\hat{G}(s)A(s)$ is then verified experimentally using FRF measurements.

3.3. Transfer function model

In section 2, the sensor and actuator dynamics of our control loop were introduced as the transfer functions $S(s)$ for the MANTIS real-time front detection and A_{D2}, A_{N2} for the deuterium and nitrogen gas valve dynamics respectively. The NII emission front response is found to be different for each actuator, so a separate transfer function models of the local plant approximation $\hat{G}_{\mathrm{D2}}(s)$ and $\hat{G}_{\mathrm{N2}}(s)$ is taken to describe the response to deuterium and nitrogen. A control-oriented transfer function model structure for emission front control in TCV was presented in [10]. This model is based on the observation of typical Warburg-domain phase and magnitude behavior of FRF measurements from D_2 gas injection to CIII front position response, indicating a (quasi) diffusive process can describe the plant dynamics.

The measured phase response to N_2 gas injection does not directly show a typical Warburg-domain behavior of roughly $-45°$ over a large frequency range. However, its magnitude response does show an equivalent slope with respect to frequency as the response to D_2. Therefore, we do reuse the (quasi) diffusive model structure here, assuming it is appropriate to describe the dynamic response to N_2 gas injection. We note, however, this choice might be overstretching the use of this model structure, but have not identified a better substantiated alternative at present.

As in [10] we take a direct relation between the change in local neutral density and front position, but allow the evaluation location of this neutral density to vary. The transfer function structure for $\hat{G}(s)$ then becomes

$$\delta y = \frac{\cosh(\hat{x}\lambda)\tanh(L\lambda) - \sinh(\hat{x}\lambda)}{D\lambda}\delta u \tag{6}$$

where $\hat{x}$, L and D represent the evaluation location, domain size and diffusion coefficient respectively, and $\lambda = \sqrt{s/D}$ with s the Laplace variable. Note that, we use here δu and δy as the model is a local (linearized) approximation of the dynamics. As the valve reference u is in units of volts, the other parameter magnitudes are no longer physical parameters, but just the structure of the function is used. One of the problems

Table 2. Plant model parameters.

Parameter	G_{N2}	G_{D2}	Unit
D	4.424	17.136	m^2s^{-1}
$\hat{x}$	0.249	0.054	m
L	0.427	2.625	m

addressed in [10] with identifying such parameters with system identification data is the limited range of frequencies that can be identified. Specifically, a lower limit is induced by the experimental time duration as discussed at the start of this section. Additional data is required to obtain a unique parameter fit, which was obtained in [10] using SOLPS-ITER simulations to obtain an additional FRF data point at the zero-frequency that represents the DC-gain. We re-use this data point, together with the conversion factor for molecules per second to volts which is different for each gas valve. The DC-gain for $\hat{G}_{D2}(s)$ then becomes 0.15 mV^{-1} corresponding to $4.22 \times 10^{-22} m/D_2 s^{-1}]$ in our operating space. For $\hat{G}_{N2}(s)$, such analysis with SOLPS-ITER has yet to be performed. We, therefore, analyze the change in NII emission front position to step-wise increases from N_2 injection in a preceeding discharge. The change in NII emission front position was 0.042 mV^{-1} for N_2 injection, which we use as the DC-gain for $G_{N2}(s)$. The resulting model parameters, after regression to the measurements, are shown in table 2. Figure 4 shows the used DC-gains by dashed lines.

Now that the individual models of the sensor, actuator and plant dynamics in the process loop in figure 1 are known from equations (1), (4) and (6), we can take their product (assuming local linearity) to obtain models for the full system as

$$\begin{aligned} \delta y_{NII} &= \underbrace{A_{N2}(s) G_{N2}(s) S(s)}_{H_{N2NII}} \delta u_{N2}(s), \\ \delta y_{NII} &= \underbrace{A_{D2}(s) G_{D2}(s) S(s)}_{H_{D2NII}} \delta u_{D2}(s). \end{aligned} \tag{7}$$

These should coincide with our FRF measurement of the full system $\hat{H}(s)$ for both cases. Figure 5 shows that this is indeed the case, as our derived transfer function models of the full system reproduces the FRF measurements, confirming that the transfer function models of (7) adequately capture the system dynamics. The transfer functions $\hat{H}_{N2NII}(s)$ and $\hat{H}_{D2NII}(s)$ may thus be used to design a controller for both actuators to control the NII emission front position in real-time. Evidently, we could have fitted a model directly from the FRF measurements of $\hat{H}(s)$, equally useful for controller design. However, separating the control loop into several sub-models provides more insight into the performance of each system component. This allows, for example, a simple replacement of the gas valve actuator model. Then, the effect of this change in actuator on control performance can be directly observed, and used to design a new controller. Furthermore, it allows the direct comparison of the measured plasma response to machines and experiments where different actuators or sensors are used.

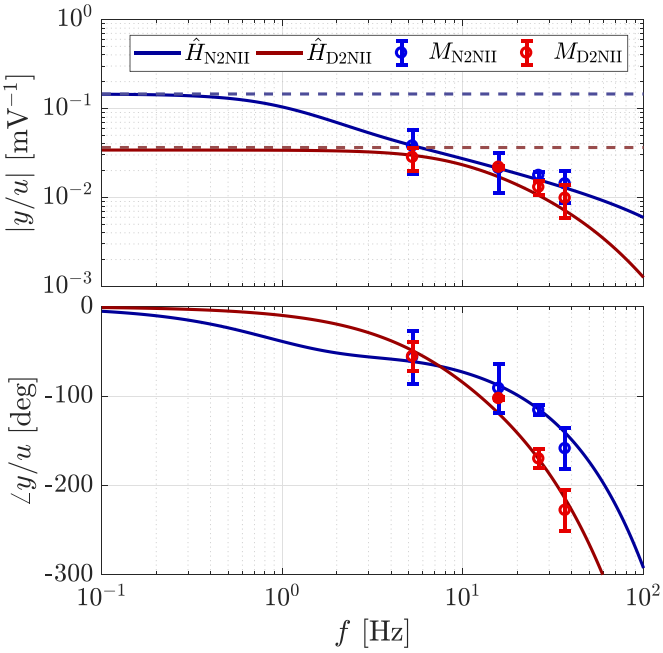


Figure 5. Bode plot of the transfer function models $\hat{H}_{N2NII}(s)$ and $\hat{H}_{D2NII}(s)$ and the FRF measurements of the full system from u (gas valve reference) to y (NII front position) in the case of D_2 and N_2 gas perturbation, indicated by $M_{D2NII}(s)$ and $M_{N2NII}(s)$ respectively. The dashed lines indicate the DC-gain used to regress the $G(s)$ models multiplied by the DC-gain of the valve and sensor, i.e. $\hat{H}_{N2NII}(0)$ and $\hat{H}_{D2NII}(0)$.

4. Control experiments

In this section, we present the NII emission front control results. We start with details on the controller design, present the experimental result for two discharges, and finally compare D_2 and N_2 actuation from two discharges with identical NII emission front position control references.

4.1. Controller design

The controllers are designed using the Loop Shaping method [20]. With this method, the loop transfer function $L(s) = \hat{H}(s)C(s)$ is shaped towards certain stability margins and performance based on the model $\hat{H}(s)$ derived in section 3. The resulting phase margin and bandwidth of a chosen controller $C(s)$ can be interpreted as a measure for stability margin and performance respectively. For reference, a phase margin of 30° is considered the minimum stability margin, while 90° is considered the most conservative. A large stability margin means the closed-loop remains stable for a large uncertainty of the model $\hat{H}(s)$, but comes at the cost of a low bandwidth and thus performance. The interested reader is referred to [6, 31] for the corresponding control theory and to [32] for a more detailed example in fusion where loop shaping was used.

As the system is gas transport driven, we do not expect any resonances and should obtain adequate performance from a PI controller. A PI controller of the form

$$C(s) = K_p \frac{s + K_i}{s} \tag{8}$$

Table 3. Controller design parameters.

Parameter	$C_{D2}(s)$	$C_{N2}(s)$	Unit
K_p	12	15	—
K_i	24π	24π	rad s^{-1}
Bandwidth	7	7	Hz
Phase margin	53	62	deg.

is chosen for both actuators, where the controller gain K_p and integrator cut-off frequency K_i are chosen such that a bandwidth of 7 Hz is obtained with a phase margin of 50° or higher to maintain sufficient robustness margin for modeling errors.

A bandwidth of 7 Hz has proven sufficient to provide reasonable performance for emission front control as shown in [7]. The controller is extended using an Infinite Impulse Response (IIR) low pass filter with a passband edge frequency at 40 Hz, to reduce the influence of high-frequency measurement noise like the measured ∼150 Hz peak originating from sawtooth crashes (see figure 4) on the tracking error. We choose an IIR low-pass filter as this meets the filter specifications with a lower filter order than Finite Impulse Response filters, leading to lower computation and storage costs in the control system [33]. The filter must be accounted for during loop shaping, by taking the product of the transfer function of the low-pass filter and the PI controller. Table 3 shows the resulting controller gains, bandwidth and phase margin.

In order to prevent integral windup, the controllers are implemented using the clamping anti-windup method. This method saturates the integral action build-up when it reaches a pre-defined threshold. This prevents overshoot caused by the rise time of a system response during which the integral action builds-up, see [34].

4.2. Experimental results

Figure 6 shows two discharges where the NII emission front position was controlled using N_2 seeding. In discharge #69144 a step-wise increase in the control reference was applied, we find the controller is able to track the desired reference well with little overshoot after the step transitions. The resulting peak target current density J_{sat}^{peak} follows an inverse response, showing a clear reduction when the NII front is at a higher position in the divertor leg. Additionally, both the total radiated power fraction P_{total}^{rad}/P_{ohm} and the radiated power fraction in the SOL P_{SOL}^{rad}/P_{SOL} show a correlated increase with NII front position height.

In discharge #69185 a step-wise increase in NII front reference position is requested first, followed by a step decrease. The controller is again well able to track the desired reference for the step increase, but the front remains too high after the step decrease, even though the controller ceases N_2 injection completely. Like the NII front position, the radiated power fractions does not decay further after 1.4 s, although, again, N_2 seeding has ceased completely. Interestingly, the peak target current density continuous to increase after this time, possibly

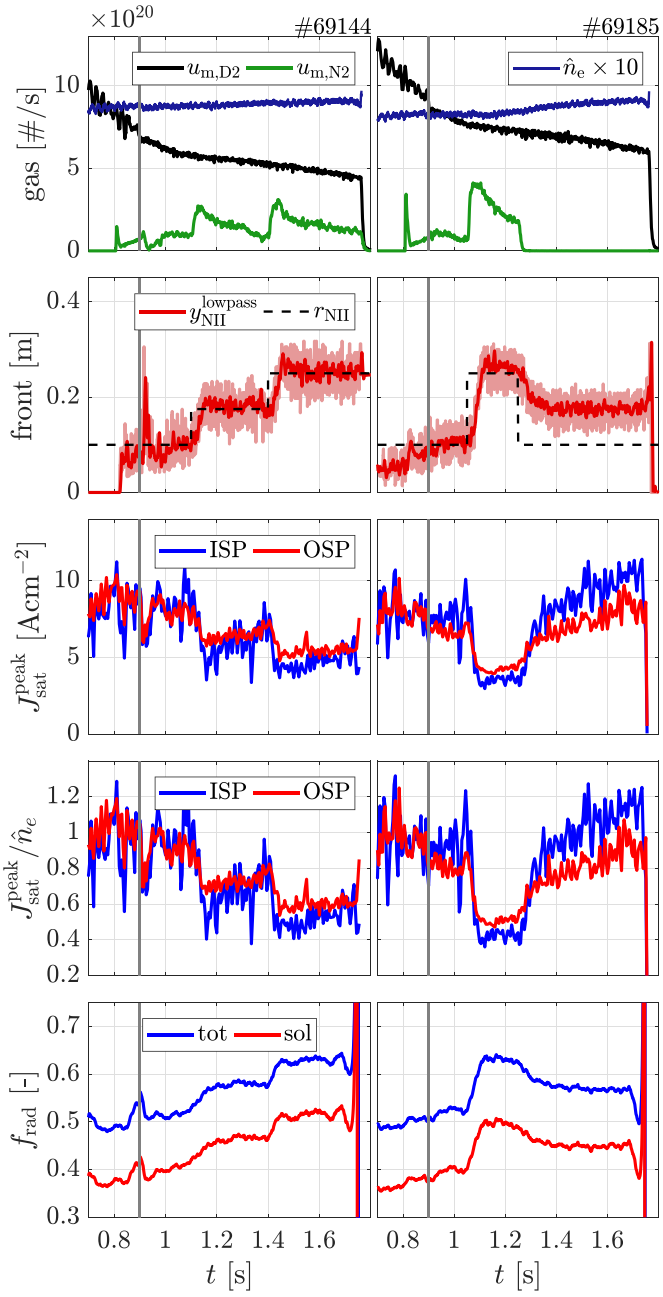


Figure 6. Experimental results for two reference tracking experiments of the NII emission front using first N_2 seeding. *Row 1:* injected N_2 and D_2 gas and line-averaged electron density $\hat{n}_e$. *Row 2:* requested front position reference r_{NII} and both raw and low-pass filtered measured front position y_{NII}. *Row 3:* peak target current density J_{sat}^{peak} on the inner strike point (ISP) and outer strike point (OSP). *Row 4:* Ratio of J_{sat}^{peak} to $\hat{n}_e \cdot 10^{19}$. *Row 5:* total radiated power fraction P_{total}^{rad}/P_{ohm} and SOL radiated power fraction P_{SOL}^{rad}/P_{SOL}.

caused by the observed increase in line-averaged density after seeding has ceased. In attached conditions of TCV L-mode plasmas, the target ion flux scales linearly with line-averaged density [13, 15]. To disentangle the effect of density changes to J_{sat}^{peak}, we analyze traces of $J_{sat}^{peak}/\hat{n}_e \cdot 10^{19}$, that show a smaller, but still clear, increase after N_2 seeding ceases.

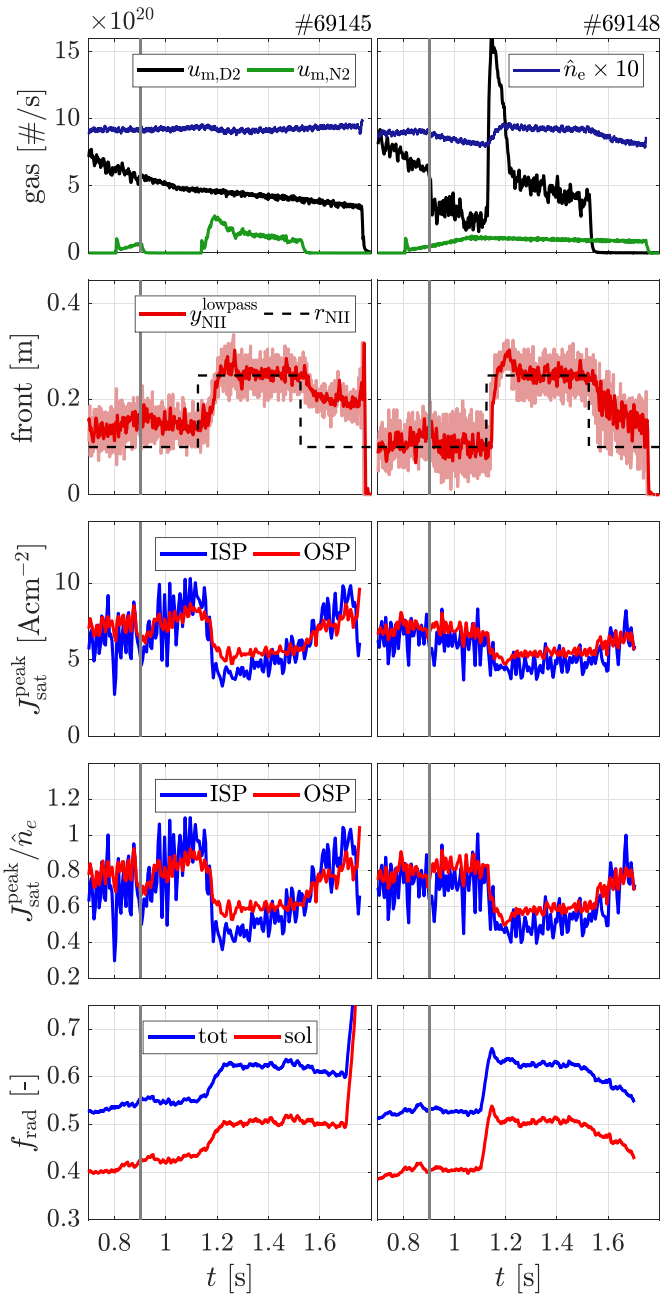


Figure 7. Experimental results for equal reference tracking of the NII emission front using N_2 (#69145) and D_2 (#69148) as an actuator. Traces as in figure 6.

4.3. Comparison of deuterium and nitrogen actuation

Figure 7 compares two discharges where the NII emission front position was controlled towards an identical reference trajectory, using N_2 seeding (#69145) or using D_2 fueling (#69148) as an actuator. With D_2 fueling a small constant influx of N_2 is maintained as a trace impurity, to ensure the NII impurity emission front can remain detectable.

The controller tracks the step-wise increase of the desired front position well for both cases. However, here again the step decrease has difficulties. For N_2 actuation the NII front position remains higher than desired, even though the N_2 valve is closed and the line-averaged electron density is no longer increasing. For D_2 actuation the NII front position again remains higher than desired, with the D_2 valve closed. Here, however, this is accompanied by a clear decrease in emission front position, in line with the decay in line-averaged density and radiated power fractions that accompany the reduced gas injection. The peak target current density $J_{\mathrm{sat}}^{\mathrm{peak}}$ shows a considerably different behavior. A clear reduction is obtained with a higher NII front position for N_2 actuation alone, which is attributed to a reduction in ionization efficiency from the SOLPS-ITER analysis in [12]. In contrast, D_2 actuation does not show this reduction. We note that moving the NII front position with D_2 actuation is coherent with the change in line-averaged density, leading to relative constant $J_{\mathrm{sat}}^{\mathrm{peak}}$, likely resulting from operating around a line-averaged density close to pre-detachment roll-over for this scenario [11]. This is confirmed by accounting for changes in line-averaged density by comparing the traces of $J_{\mathrm{sat}}^{\mathrm{peak}}/\hat{n}_{\mathrm{e}}$, showing fairly similar changes for both D_2 and N_2 actuation.

5. Conclusion and discussion

In this work, we have shown the first results of real-time control of the NII (399.5 nm) emission front position using N_2 seeding in TCV, diagnosing the exhaust plasma by using light emission of an injected impurity gas. We used a novel control-oriented transfer function structure for emission front control in TCV [10], regressed onto system identification measurements to obtain a (locally valid) dynamic model of the NII front response to both D_2 and N_2 gas injection. This model was combined with an identified model for the gas valve actuators, and for the MANTIS sensor, to construct a model description of the complete system dynamics, subsequently used to design controllers off-line, providing successful control of the following discharge.

We have demonstrated real-time control of the NII emission front position actuated by N_2 gas injection, or actuated by D_2 gas injection while injecting a small amount of N_2 as a trace impurity. For both cases, the NII emission front was controlled towards higher positions, but moving the front position back towards the target proved difficult, likely affected by nitrogen retention in the machine. This retention was observed to affect subsequent discharges, showing the importance of tracking impurity retention and efficiently removing impurities from the machine. If impurity injection is used to mitigate radiative fluctuations in the plasma exhaust this accumulation would become a limiting factor in control performance, strategies where impurity injection is kept to a minimum would be required. This is in line with the strategic operation of exhaust control, that must simultaneously encompass a soft limit of re-attachment (which can still be temporarily endured by using, for example, strike-point sweeping [35–37]), and a hard limit resulting from radiative instability induced disruptions.

We found the NII front position is consistently located between the CIII emission front and the divertor target, showing the NII front position is indicative of a colder plasma region than its CIII counterpart. This is qualitatively in line with the SOLPS-ITER analysis of [12], where the CIII and

NII impurity emission front was found to correspond to a local electron temperature of 11–12 and 6.5 eV respectively, where it should be recalled that experimental measurements of the CIII emission front temperature are considerably lower (see e.g. [13]). We have shown the CIII and NII emission front positions respond simultaneously to the injection of D_2 or N_2 perturbations in the described system identification experiments, indicating these front positions cannot be controlled independently by the used actuators, at least up to the highest probed excited frequency of 37 Hz. Additionally, this result highlights the robustness of using these emission fronts as an indication of local electron temperature, where the amount of emitting impurities, injected or sputtered, seems to not significantly affect the location of their emission.

However, both emission fronts do respond differently to D_2 actuation than to N_2 actuation, where the latter induces a stronger, but slower response of both front positions. We note that N_2 is injected in the private flux region, while D_2 is injected in the open flux region, possibly partly explaining the difference in response. However, the frequency response measurements in [7] using D_2 injection in the private flux region show similar results as the results of D_2 injection presented here. This leads us to conjecture that differences in transport and thermal velocity due to mass difference may be a more reasonable candidate to explain this difference in response, but further investigation is necessary.

We note that, even after completely ceasing N_2 or D_2 injection, pre-seeding/fueling conditions were not obtained before the end of the discharge, likely caused by insufficient N_2 impurity removal and/or decay-time of divertor plasma density, respectively. However, [7] demonstrated the displacement of the CIII emission front from the target and back twice using D_2 in an unseeded TCV discharge with a similar controller, showing faster movement of an impurity emission front back to the target than observed in this work. Leaving one of the actuators (N_2 or D_2) uncontrolled may be the cause of this discrepancy, unintentionally increasing impurity enrichment in the case of D_2 actuation instead of merely having a trace impurity. A combination of real-time D_2 and N_2 actuation to control the divertor state more appropriately may be required, complemented by an additional measurement next to an impurity emission front position, for example tracking impurity retention. As both D_2 injection and N_2 injection affect the impurity emission front position in different ways, this will require a controller that specifically handles this interaction. Such a multi-input multi-output controller is presently under development at TCV.

Acknowledgments

DIFFER is part of the institutes organization of NWO.

This work was supported in part by the Swiss National Science Foundation.

This work has been carried out within the framework of the EUROfusion Consortium, funded by the European Union via the Euratom Research and Training Programme (Grant Agreement No. 101052200—EUROfusion). Views and opinions expressed are however those of the author(s) only and do not necessarily reflect those of the European Union or the European Commission. Neither the European Union nor the European Commission can be held responsible for them.

ORCID iDs

J.T.W. Koenders https://orcid.org/0000-0003-4385-923X
A. Perek https://orcid.org/0000-0002-4117-0298
B. Kool https://orcid.org/0000-0002-1636-7400
O. Février https://orcid.org/0000-0002-9290-7413
T. Ravensbergen https://orcid.org/0000-0001-7347-5515
C. Theiler https://orcid.org/0000-0003-3926-1374
M. van Berkel https://orcid.org/0000-0001-6574-3823

References

[1] Zohm H. *et al* 2013 On the physics guidelines for a tokamak DEMO *Nucl. Fusion* **53** 073019
[2] Loarte A. *et al* 2007 Progress in the ITER physics basis chapter 4: power and particle control *Nucl. Fusion* **47** 203
[3] Pitts R.A. *et al* 2019 Physics basis for the first ITER tungsten divertor *Nucl. Mater. Energy* **20** 100696
[4] Lipschultz B., Parra F.I. and Hutchinson I.H. 2016 Sensitivity of detachment extent to magnetic configuration and external parameters *Nucl. Fusion* **56** 056007
[5] Donné T. 2018 European research roadmap to the realisation of fusion energy *EUROfusion*
[6] Franklin G.F. *et al* 2019 *Feedback Control of Dynamical Systems* 8th edn (New York: Pearson)
[7] Ravensbergen T. *et al* 2021 Real-time feedback control of the impurity emission front in tokamak divertor plasmas *Nat. Commun.* **12** 1–9
[8] Kallenbach A. *et al* 2013 Impurity seeding for tokamak power exhaust: from present devices via ITER to DEMO *Plasma Phys. Control. Fusion* **55** 124041
[9] Guillemaut C. *et al* 2017 Real-time control of divertor detachment in H-mode with impurity seeding using Langmuir probe feedback in JET-ITER-like wall *Plasma Phys. Control. Fusion* **59** 1–7
[10] Koenders J., Wensing M., Ravensbergen T., Février O., Perek A. and van Berkel M. (The TCV Team and The EUROfusion MST1 Team) 2022 Systematic extraction of a control-oriented model from perturbative experiments and SOLPS-ITER for emission front control in TCV *Nucl. Fusion* **62** 066025
[11] Février O. *et al* 2020 Nitrogen-seeded divertor detachment in TCV L-mode plasmas *Plasma Phys. Control. Fusion* **62** 035017
[12] Smolders A. *et al* 2020 Comparison of high density and nitrogen seeded detachment using SOLPS-ITER simulations of the tokamak á configuration variable *Plasma Phys. Control. Fusion* **62** 125006
[13] Theiler C. *et al* 2017 Results from recent detachment experiments in alternative divertor configurations on TCV *Nucl. Fusion* **57** 072008
[14] Reimerdes H. *et al* 2022 Overview of the TCV tokamak experimental programme *Nucl. Fusion* **62** 042018
[15] Verhaegh K. *et al* 2019 An improved understanding of the roles of atomic processes and power balance in divertor target ion current loss during detachment *Nucl. Fusion* **59** 126038

[16] Perek A. *et al* 2021 Measurement of the 2D emission profiles of hydrogen and impurity ions in the TCV divertor *Nucl. Mater. Energy* **26** 100858
[17] Perek A. *et al* 2022 A spectroscopic inference and SOLPS-ITER comparison of flux-resolved edge plasma parameters in detachment experiments on TCV *Nucl. Fusion* **62** 096012
[18] Harrison J.R. *et al* 2017 Detachment evolution on the TCV tokamak *Nucl. Mater. Energy* **12** 1071–6
[19] Harrison J.R. *et al* 2019 Progress toward divertor detachment on TCV within H-mode operating parameters *Plasma Phys. Control. Fusion* **61** 065024
[20] Skogestad S. and Postlethwaite I. 2007 *Multivariable Feedback Control—Analysis and Design* 2nd edn (New York: Wiley)
[21] Ravensbergen T., van Berkel M., Silburn S.A., Harrison J.R., Perek A., Verhaegh K., Vijvers W.A.J., Theiler C., Kirk A. and de Baar M.R. (The EUROfusion MST1 Team) 2020 Development of a real-time algorithm for detection of the divertor detachment radiation front using multi-spectral imaging *Nucl. Fusion* **60** 066017
[22] Perek A. *et al* 2019 MANTIS: a real-time quantitative multispectral imaging system for fusion plasmas *Rev. Sci. Instrum.* **90** 123514
[23] Furno I., Weisen H., Mlynar J., Pitts R.A., Llobet X., Marmillod P. and Pochon G.P. 1999 Fast bolometric measurements on the TCV tokamak *Rev. Sci. Instrum.* **70** 4552–6
[24] Février O., Theiler C., De Oliveira H., Labit B., Fedorczak N. and Baillod A. 2018 Analysis of wall-embedded Langmuir probe signals in different conditions on the tokamak à configuration variable *Rev. Sci. Instrum.* **89** 053502
[25] Bates S.C. and Burrell K.H. 1984 Fast gas injection system for plasma physics experiments *Rev. Sci. Instrum.* **55** 934–9
[26] Hespanha J. 2009 *Linear Systems Theory* (Princeton, NJ: Princeton University Press)
[27] van Berkel M. *et al* 2020 Correcting for non-periodic behaviour in perturbative experiments: application to heat pulse propagation and modulated gas-puff experiments *Plasma Phys. Control. Fusion* **62** 094001
[28] Pintelon R. and Schoukens J. 2012 *System Identification—A Frequency Domain Approach* 2nd edn (Hoboken, NJ: John Wiley and Sons)
[29] Pintelon R., Schoukens J., Pauwels L. and Van Gheem E. 2005 Diffusion systems: stability, modeling and identification *Ontario, Canada (16-19 May 2005) IEEE Instrumentation and Measurement Technology Conf. Proc.* vol 2 pp 894–9 (https://doi.org/10.1109/imtc.2005.1604264)
[30] van Berkel M. Eindhoven University of Technology 2015 Estimation of heat transport coefficients in fusion plasmas *PhD Thesis* (available at: https://research.tue.nl/en/publications/estimation-of-heat-transport-coefficients-in-fusion-plasmas)
[31] Bruijnen D., van de Molengraft R. and Steinbuch M. 2006 Optimization aided loop shaping for motion systems *Germany. Munich (October 4-6, 2006) 2006 IEEE Conf. on Computer Aided Control System Design, 2006 IEEE Int. Conf. on Control Applications, 2006 IEEE Int. Symp. on Intelligent Control* (IEEE) pp 255–60 (https://doi.org/10.1109/CACSD-CCA-ISIC.2006.4776655)
[32] Witvoet G. *et al* 2011 Systematic design of a sawtooth period feedback controller using a Kadomtsev–Porcelli sawtooth model *Nucl. Fusion* **51** 073024
[33] Sutradhar S.R., Sayadat N., Rahman A., Munira S., Fazlul Haque A.K.M. and Sakib S.N. 2017 IIR based digital filter design and performance analysis *(10-11 August, 2017) 2017 2nd Int. Conf. Telecommunication and Networks (TEL-NET)* vol 2018 (IEEE) pp 1–6 (https://doi.org/10.1109/TEL-NET.2017.8343596)
[34] Åström K.J. and Hägglund T. 2006 *Advanced PID Control* (Research Triangle Park, NC: ISA—The Instrumentation, Systems and Automation Society)
[35] Maddison G. *et al* 2011 Demonstration of real-time control of impurity seeding plus outboard strike-point sweeping in JET ELMy H-mode plasmas *Nucl. Fusion* **51** 082001
[36] Horacek J., Cunningham G., Entler S., Dobias P., Duban R., Imrisek M., Markovic T., Havlicek J. and Enikeev R. 2017 Feasibility study of fast swept divertor strike point suppressing transient heat fluxes in big tokamaks *Fusion Eng. Des.* **123** 646–9
[37] Horacek J., Lukes S., Adamek J., Havlicek J., Entler S., Seidl J., Cavalier J., Cikhardt J. and Sedmidubsky V. 2022 Novel concept suppressing plasma heat pulses in a tokamak by fast divertor sweeping *Sci. Rep.* **12** 17013